



Micro Flower-Like Hierarchical Mo₂C/Co@NC (N-Doped Carbon) for Efficient Bifunctional Electrocatalyst

Hee Soo Kim¹ · Ahyoun Lim² · Mino Woo^{1,3} · Hae In Lee¹ · Yunjang Gu¹ · Dong-Ha Lim¹

Received: 3 May 2023 / Revised: 28 September 2023 / Accepted: 29 September 2023 / Published online: 30 January 2024
© The Author(s), under exclusive licence to Korean Institute of Chemical Engineers, Seoul, Korea 2024

Abstract

The development of low-cost and high-efficiency electrocatalysts for the water-splitting reaction to produce oxygen and hydrogen from alkaline electrolytes remains a major challenge, especially from the perspective of realizing fast and efficient oxygen evolution reaction (OER) and hydrogen evolution reaction (HER) catalysts, and it is important to improve the performance of these reactions through rational catalyst design. In this study, Co-based heterostructures composed of cobalt (Co) and molybdenum carbide (Mo₂C) nanoparticles with micro-flower-like structures were intentionally designed as precursors for OER and HER electrocatalysts. In particular, during polymerization, nanoparticle (metal precursor) ions and dopamine aggregates combined to grow into nano-flakes and retained their structure after carbonization, forming micro-flower-like structures characterized by high specific surface area and porosity. The catalysts with hierarchical heterostructures constructed using this unique structure showed activities similar to those of the commercially available IrO₂ and Pt/C catalysts, reaching current densities of 10 mA/cm² for OER and HER in 0.1 M KOH and exhibiting good durability. Therefore, our results present new concepts for the structuring and fabricating catalysts to realize efficient OER and HER kinetics, and we expect that they will be utilized in the energy conversion field.

Keywords Mo₂C/Co composite structure · OER · HER · N-doped carbon · Micro flower-like structure

Introduction

Electrocatalytic splitting of water into hydrogen and oxygen is an extremely important reaction in energy conversion systems. However, because of the slow kinetic nature of the hydrogen evolution reaction (HER) and oxygen evolution reaction (OER), electrocatalysis is required to overcome the kinetic barrier [1–4]. Nanoparticles and compounds of precious metals, such as platinum, ruthenium, and iridium, are

state-of-the-art electrocatalysts, but their scarcity and high cost are major obstacles to their widespread use in commercial applications [5–8]. Although considerable effort has been dedicated toward studying transition-metal-nanoparticle (i.e., Co, Ni, Fe, Mo)-based catalysts, including nanoparticle carbides, nitrides, chalcogenides, oxides/hydroxides, and phosphides, research on transition-nanoparticle-based catalysts for the HER and OER remains scarce compared to that on noble-metal-nanoparticle-based catalysts owing to their different electrocatalytic kinetics and electron-transfer steps [7, 9–11]. These reasons make it difficult to commercially apply transition metal nanoparticles to water-splitting electrolytes. Therefore, the development of high-performance catalysts for total water splitting has attracted considerable attention from researchers.

Among the existing non-noble nanoparticle catalysts, molybdenum carbide (Mo₂C) has received special attention owing to its Pt-like electronic properties [12–14]. In recent years, Mo₂C has attracted significant attention as an HER catalyst because of its Pt-like d-band electronic structure, high electronic conductivity, and excellent corrosion resistance [13, 15, 16]. Therefore, although Mo₂C-based materials

✉ Hee Soo Kim
catacylsm@kitech.re.kr

✉ Dong-Ha Lim
dongha4u@kitech.re.kr

¹ Green Materials and Processes R&D Group, Korea Institute of Industrial Technology (KITECH), Ulsan 44413, Republic of Korea

² Hydrogen Fuel Cell Research Center, Korea Institute of Science and Technology (KIST), Seoul 02792, Republic of Korea

³ Department of Mechanical Engineering, Korea Maritime and Ocean University, Busan 49112, Republic of Korea

with high HER activity have been widely reported for the aforementioned reasons, the OER-associated catalytic activity of Mo_2C alone is not as good as that of noble metal-based materials because of its low electrical conductivity and slow interfacial reaction rate. To compensate for this drawback, transition nanoparticles such as Ni, Co, Fe, and Cu can be used to promote its water-splitting catalytic activity because the combination of Mo_2C with electron-rich transition metals further reduces the number of free *d* orbitals in the Mo species [13, 14, 17]. Thus, the hydrogen adsorption performance on the Mo_2C surface is properly regulated (optimizes for the hydrogen to adhere to the surface) and the H_2 gas generation performance is improved. For this reason, a few recent studies have demonstrated that combining Mo_2C with transition nanoparticles can be an effective approach to improve OER performance. According to Yu et al. and Liang et al., Ni/ Mo_2C nanorods and Mo_2C -coated carbon nitride and Co nanoparticles have small overpotentials of 179 mV in the HER and 368 mV in the OER, as well as overpotentials of 99 mV and 347 mV in the HER and OER, respectively, and a current density of 10 mA/cm² [18, 19]. Although the reported OER/HER properties of Mo_2C catalysts can be improved to some extent, several key issues need to be addressed. First, nano-sized Mo_2C is prone to agglomeration or disproportionate growth because of the relatively high calcination temperature encountered during synthesis, which decreases the active surface area and degrades OER performance [19–21]. In addition, the durability of Mo_2C -based electrocatalysts is short from the perspective of their use in practical applications [22–24]. Therefore, efficient design and controllable synthesis of unique Mo_2C -based catalysts that bind strongly to active HER and OER centers, have abundant exposed active sites, fast charge transfer kinetics, and good structural stability remain challenges in realizing high-efficiency water splitting.

In this paper, we report a porous nitrogen-doped composite composed of carbon-wrapped $\text{Mo}_2\text{C}/\text{Co}@N\text{-C}$ catalyst synthesized using polymerization and subsequent pyrolysis. Owing to the formation of complexes between nanoparticle (metal precursor) ions and dopamine, these complexes grow into nanoflake-like structures, forming a micro-flower-like shape with a high specific surface area and porosity. In addition, utilizing a facile thermal process, these nanoparticle-dopamine nanosheets can be converted into microscopic Mo_2C and Co nanoparticles, where the isolated Mo_2C and Co act as catalysts to simultaneously form a graphene layer. The in situ generated and uniformly dispersed nanoscale Co nanoparticles and Mo_2C ensure a strong binding effect and improve the efficiency of both the OER and HER. The carbon layer not only stabilizes the structure and protects Co and Mo_2C from alkaline corrosion but also enhances electron transfer between the carbon layer and these nanoparticles. Moreover, dopamine offers the advantages of

simple synthesis and good environmental stability, and it is one of the most widely studied polymer precursors. During pyrolysis, dopamine can be converted to nitrogen-doped carbon. Some of this carbon decomposes into a gaseous form, creating a porous structure. The introduction of these nitrogen-doped carbon materials enhances electron transfer and electrical conductivity in the electrocatalytic process. For this reason, transition nanoparticle/carbon-based electrocatalysts provide bifunctional activity. Their hierarchical structure provides more active surface sites, improves electrode–electrolyte interfacial contact, and maintains their structural stability and integrity. Consequently, the synthesized $\text{Mo}_2\text{C}/\text{Co}@N\text{-C}$ catalysts exhibit good activity in both HER and OER under alkaline electrolyte conditions (0.1 M KOH) and possess excellent stability.

Experimental

Chemicals and Reagents

Sodium molybdate ($\text{Na}_2\text{MoO}_4 \cdot 2\text{H}_2\text{O}$, 99.5%), cobalt(II) nitrate hexahydrate ($\text{Co}(\text{NO}_3)_2 \cdot 6\text{H}_2\text{O}$, 98%), 20 wt% Pt/C, Nafion perfluorinated resin solution (5 wt%), and dopamine hydrochloride were purchased from Sigma-Aldrich company. Deionized (DI) water, EtOH (99%), and NH_4OH (28%) were purchased from DaejungChem company. IrO_2 (99.99%) was obtained from Alfa Aesar. All reagents were used without further purification.

Synthesis of $\text{Mo}_2\text{C}@N\text{-C}$ and $\text{Mo}_2\text{C}/\text{Co}@N\text{-C}$ Catalysts

First, 1.02 g of sodium molybdate and 0.32 g of dopamine hydrochloride were added to 20 ml of EtOH and 70 ml of DI water. This mixture was stirred at 1000 rpm for 60 min until a homogenous solution was obtained. Close to the end of stirring, 0.31 g of cobalt(II) nitrate hexahydrate was added in, and the solution was stirred for an additional 10 min. Thereafter, 0.25 ml of 28% ammonia solution was added to the solution, and the polymerization reaction was conducted at room temperature for 12 h at 1000 rpm. A centrifuge was then used to recover the synthesized polymer, which was washed with water and ethanol. The electrocatalyst was synthesized using a thermal reaction at 800 °C for 90 min in a nitrogen atmosphere (ramping rate: 8.5 °C/min). To prepare the $\text{Mo}_2\text{C}@N\text{-C}$ catalyst, the same process was followed, except for the addition of cobalt(II) nitrate hexahydrate.

Electrochemical Measurements

Catalytic inks were prepared by mixing 10 mg of $\text{Mo}_2\text{C}@N\text{-C}$ or $\text{Mo}_2\text{C}/\text{Co}@N\text{-C}$ catalyst with 100 μl of

naphtha resin solution and 1 mL of isopropyl alcohol (IPA), followed by sonication. The inks were deposited on a glassy carbon electrode (GC area = 0.19625 cm²) with a loading of 0.232 mg/cm². The OER activities of the catalysts were compared using commercial Pt/C and IrO₂ catalysts as reference catalysts at a loading of 0.232 mg/cm². All electrochemical measurements in this study were performed at 298 K using Autolab in a three-electrode cell configuration with a saturated Ag/AgCl reference electrode and a Pt wire as the counter electrode. Linear sweep voltammetry (LSV) measurements of the OER and HER were performed under the following conditions: scan rate of 5 mV/s, room temperature, 1600 rpm, and 0.1 M KOH. For long-term performance testing, we tested the Mo₂C/Co@N-C catalyst at 1600 rpm for 12 h at a current density of 10 mA/cm². Moreover, all measurements were performed by returning all potentials to that of a reversible hydrogen electrode ($E_{\text{RHE}} = E_{\text{Ag/AgCl}} + 0.059 \text{ pH} + 0.197 \text{ V}$). To measure the electrochemical surface area (ECSA) of the catalysts, each of the catalysts was loaded onto separate glassy carbon electrodes (0.232 mg/cm²), and their cyclic voltammograms (CV) were obtained at scan rates of 10–100 mV/s scan rate in the non-Faradaic range (1.1–1.25 V_{RHE}). Electrochemical impedance spectroscopy (EIS) spectra were recorded at the open circuit potential with an alternating perturbation of 10 mV and a frequency range of 100 kHz to 0.01 Hz. All electrochemical data were reported without iR compensation.

Material Characterizations

X-ray diffraction (XRD) spectra were recorded using a Rigaku (MiniFlex-2) equipped with a Cu K α radiation source ($\lambda = 1.5406 \text{ \AA}$). Scanning electron microscopy (SEM) and energy dispersive X-ray spectrometer (EDS) mapping images were obtained using an Inspect F50 microscope with an accelerating voltage of 10 kV. X-ray photoelectron

spectroscopy (XPS) spectra were acquired using a PHI Versa Probe system equipped with a 100-W Al K α X-ray source. Transmission electron microscopy (TEM) images were recorded using a transmission electron microscope (TitanTM 80–300). Low-temperature N₂ sorption isotherms were recorded at 77 K

using a BEL Mini adsorption volumetric analyzer (BEL, Inc., Japan). All samples were degassed at 393 K for 12 h under a static vacuum before conducting adsorption measurements. The specific surface area (SSA) of the samples was determined using the Brunauer–Emmett–Teller (BET) method for the nitrogen adsorption isotherms in the relative pressure (P/P_0) range of 0.05–0.20. Pore size distribution (PSD) was determined using the Barrett–Joyner–Halenda (BJH) method. The total pore volume was obtained at 0.99 P/P_0 . Thermogravimetric analysis (TGA) was performed using an SDT Q600 device (TA Instruments Inc., New Castle, DE).

Results and Discussion

As shown in Fig. 1, dopamine initiates a polymerization reaction under basic conditions to form 5,6-dihydroxyindole, which grows into nano-flakes as the nanoparticle ions combine with the oxygen in the hydroxy. These flakes then grow and aggregate to form micro-flowers (Fig. S1) [25, 26], which retain their shape even after carbonization. In addition, during pyrolysis, a portion of the polymer composed of polydopamine is pyrolyzed. Consequently, the polymer skeleton collapses, and small pores are formed, which decreases the overall particle size but increases the surface area. FE-SEM images of the Mo₂C/Co@N-C and Mo₂C@N-C catalysts were obtained, as illustrated in Figs. 2 and S2a. The as-prepared Mo₂C/Co@N-C samples are composed of micro-flower-shaped spherical particles with a corrugated

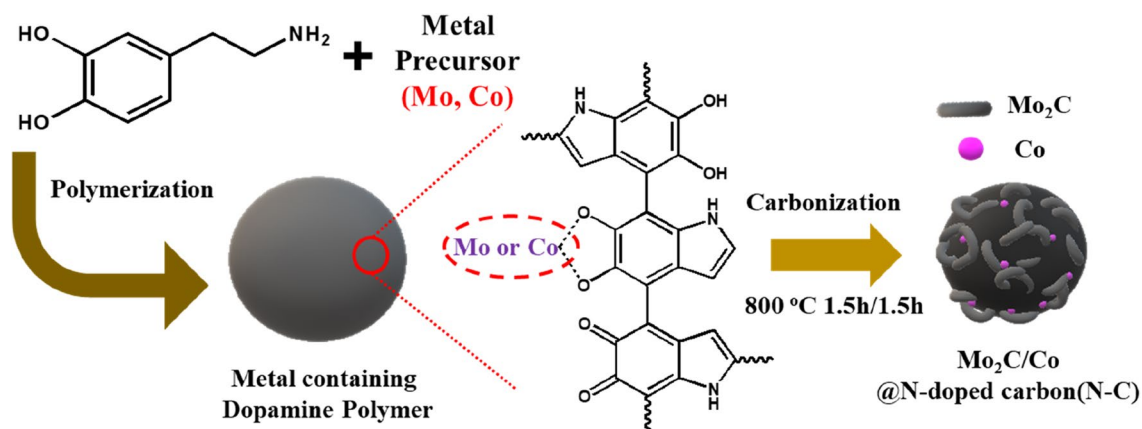


Fig. 1 Schematic illustration of Mo₂C/Co@N-C (N-doped carbon) fabrication

surface, and their sizes range from a few to tens of μm . The Co nanoparticle is present in the interstices between the corrugated structures. The $\text{Mo}_2\text{C}@N\text{-C}$ catalyst has a wrinkled morphology, and its surface particle size is similar to that of $\text{Mo}_2\text{C}/\text{Co}@N\text{-C}$. However, its surface is smoother than that of $\text{Mo}_2\text{C}@N\text{-C}$ owing to the presence of Co particles (Figs. S2b and c).

Furthermore, as depicted in the EDS elemental map in Fig. 2b, the elements Mo, Co, N, and C are present and uniformly distributed throughout the prepared $\text{Mo}_2\text{C}/\text{Co}@N\text{-C}$. The high-resolution TEM images in Fig. 2c and d show tens of nm-sized Mo_2C and Co nanoparticles dispersed uniformly in the N-doped carbon matrix in the form of flakes and wrinkles, as observed in the SEM images. In addition, the nanoparticles have lattice fringes of 0.238 and 0.244 nm, which correspond to the (101) and (111) planes of Mo_2C and Co nanoparticles, respectively [18, 27, 28]. In particular, in the inset image of Fig. 2d, graphene can be observed around the periphery because of the formation of Mo_2C and Co nanoparticles when the polymer is converted to carbon during the carbonization process; this carbon acts as a catalyst that facilitates the formation of graphene structures on the surface of these metal particles, as has been reported in

several previous studies [29–31]. This means that the $\text{Mo}_2\text{C}/\text{Co}@N\text{-C}$ catalyst possesses high electrical conductivity because of the aforementioned graphene structure.

The XRD pattern of $\text{Mo}_2\text{C}/\text{Co}@N\text{-C}$ is depicted in Fig. 3a. The green circled area corresponds to hexagonal $\beta\text{-Mo}_2\text{C}$ (PDF number 35–0787), and the purple circled area corresponds to cubic Co (PDF number 15–0806) [19, 20, 32]. For $\text{Mo}_2\text{C}@N\text{-C}$, except for the Co particles, the other particles had the same $\beta\text{-Mo}_2\text{C}$ -associated XRD peak (see the green and purple circled portion) as that of $\text{Mo}_2\text{C}/\text{Co}@N\text{-C}$. In addition, XRD confirms that Mo_2C and Co are present in the graphite carbon as seen in the previous TEM analysis [29, 30]. Interestingly, XRD peaks related to MoC were also observed (sky-blue circles) [29, 30]. However, this study will discuss the impact of Mo_2C and Co on OER and HER rather than MoC as they are present in small proportions as can be seen from the XRD results. Hence, these XRD results confirm the successful formation of Mo_2C and Co inside the carbon, which is consistent with the SEM/TEM results. To observe the physical properties of $\text{Mo}_2\text{C}/\text{Co}@N\text{-C}$ and $\text{Mo}_2\text{C}@N\text{-C}$ catalysts prepared using carbonization and the differences with and without Co, N_2 adsorption data were analyzed to obtain the SSA and

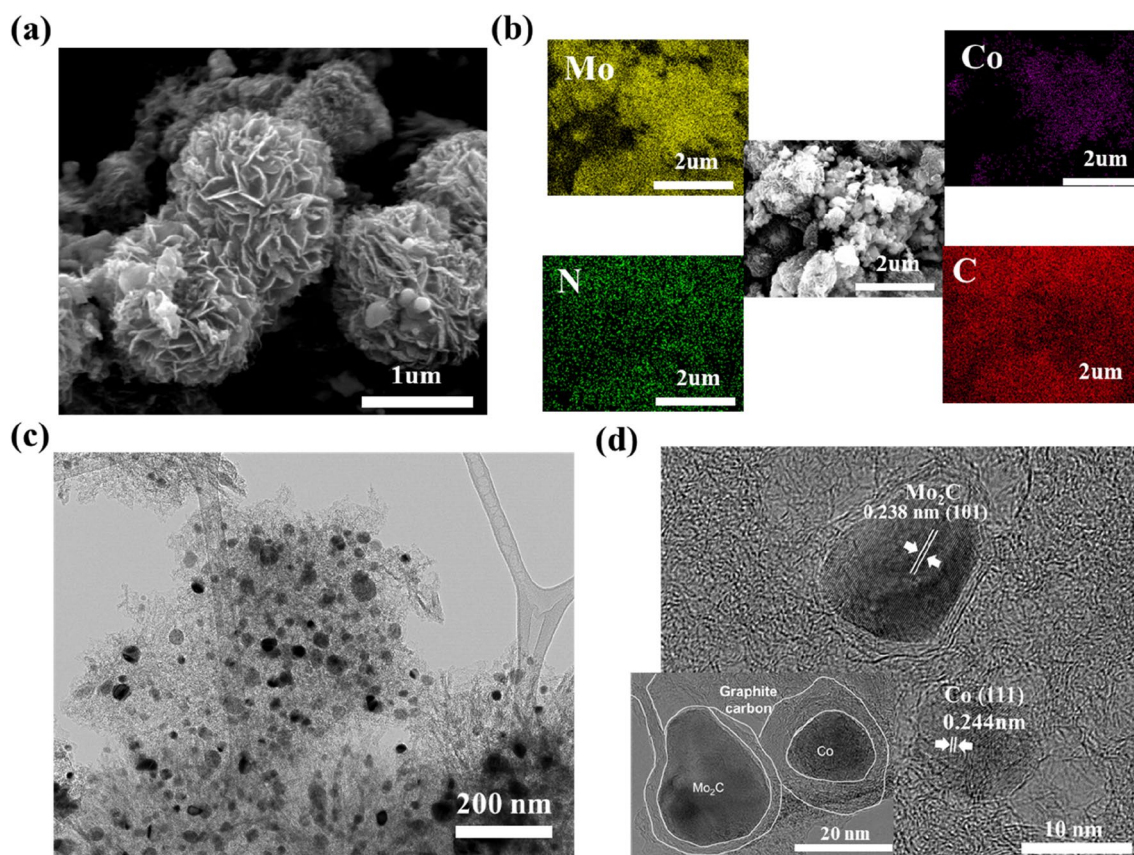


Fig. 2 SEM image (a) and EDS mapping images (b) of $\text{Mo}_2\text{C}/\text{Co}@N\text{-doped carbon}$. TEM images (c and d) of $\text{Mo}_2\text{C}/\text{Co}@N\text{-doped carbon}$. The inset of d is an enlarged view of the Co nanoparticles in the $\text{Mo}_2\text{C}/\text{Co}@N\text{-doped carbon}$ catalyst

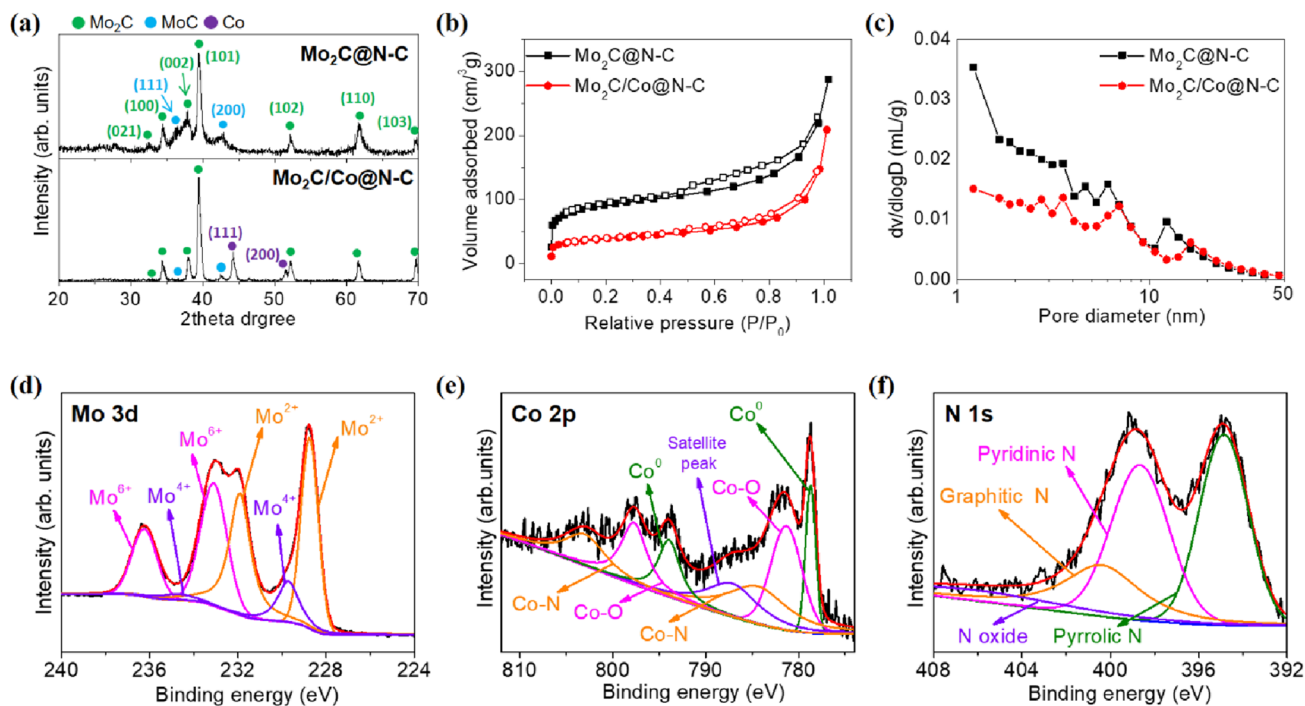


Fig. 3 XRD patterns of Mo₂C@N-C and Mo₂C/Co@N-C samples (a). N₂ sorption (b) and BJH plot (c) of Mo₂C@N-C and Mo₂C/Co@N-C samples. High-resolution Mo 3d, Co 2p, and N 1s spectra were acquired using Mo₂C/Co@N-C sample (d, e)

the BJH PSDs. As shown in Fig. 3b, the Mo₂C/Co@N-C and Mo₂C@N-C catalysts exhibited hysteresis loops corresponding to a type IV isotherm at relative pressures of 0.4–0.99 (P/P_0). These mesopores were formed during the formation of Mo, Co ions in Mo₂C, and Co particles during carbonization, as well as during the collapse of the polymer structure owing to carbonization. Furthermore, due to the hierarchical structure of highly interconnected micropores (see Fig. 3c), as seen in the N₂ adsorption results, the Mo₂C/Co@N-C electrocatalyst shows H3-type hysteresis loops close to cylindrical and slit-like pore structures. The SSA values of the Mo₂C@N-C and Mo₂C/Co@N-C catalysts were 320 and 141 m²/g, respectively, and their total pore volumes were 0.37 and 0.2 cm³/g. The SSA and total pore volume of Mo₂C/Co@N-C were expected to be lower than those of Mo₂C@N-C without Co nanoparticles because the Co nanoparticles blocked the pores present inside the carbon. Moreover, all catalysts exhibited a pore structure with pores ranging in size from 2 to 10 nm, as can be inferred from the BJH plots. Consistent with the N₂ sorption results, in the BJH results, Mo₂C/Co@N-C had fewer mesopores in the presence of Co. Moreover, according to the TGA results obtained in the air atmosphere, the percentages of Mo₂C/Co and carbon were 39% and 61%, respectively (Fig. S3).

XPS analyses of Mo 3d, Co 2p, and N 1s were performed to further study the chemical bonding information

of the Mo₂C/Co@N-C catalyst (Figs. 3d–f and S4). First, according to the XPS survey scan results depicted in Fig. S4, the Mo₂C:Co ratio was roughly 2.2:1 (wt%) and 1.8:1 (at%). Mo 3d was decomposed into three peaks corresponding to Mo²⁺, Mo⁴⁺, and Mo⁶⁺ [19, 20]. Among them, the peak corresponding to Mo²⁺ was assigned to carbides. In particular, Mo²⁺ can be attributed to Mo₂C, which is beneficial for HER and OER because it increases the number of active sites on the material surface and improves electron density [14, 16, 17].

In addition, Mo⁴⁺ and Mo⁶⁺ were thought to have originated from MoO₃ owing to surface oxidation during synthesis or exposure to air [33–36]. For Co 2p, the peaks at 784.8 and 804.1 eV corresponded to Co–N, which can be very beneficial for increasing catalytic activity, and many studies have demonstrated that catalytic nanoparticles coated with N-doped carbon materials can improve catalytic activity, stability, and electroconductivity [19, 20, 32]. However, the peaks at 772, 778, 793, and 797 eV can be attributed to the oxidation of the cobalt surface [37–40]. For N 1s, the peaks assigned to pyridinic-N (ca. 398 eV), pyrrolic-N (ca. 395 eV), graphitic-N (ca. 401 eV), and N oxide (ca. 405 eV) were deconvoluted [41–45]. Interestingly, pyridinic-N, pyridinic-N, and graphite-N can provide more active sites, higher electron conduction, and greater stability during electrochemical processes [13, 26,

31], as mentioned earlier. The results of these XPS analyses agree well with the SEM and TEM results.

The OER activities of $\text{Mo}_2\text{C}/\text{Co}@N\text{-C}$, $\text{Mo}_2\text{C}@N\text{-C}$, and commercial IrO_2 catalysts were investigated in a 0.1 M KOH aqueous solution (Fig. 4a, b). The OER polarization curves are depicted in Fig. 4a. $\text{Mo}_2\text{C}/\text{Co}@N\text{-C}$ requires a potential of $1.61 V_{\text{RHE}}$ to reach $10 \text{ mA}/\text{cm}^2$, which is similar to that of commercial IrO_2 ($1.60 V_{\text{RHE}}$). In contrast, $\text{Mo}_2\text{C}@N\text{-C}$ requires a higher potential ($1.75 V_{\text{RHE}}$) than the two catalysts mentioned in the preceding sentence. This result indicated that $\text{Mo}_2\text{C}/\text{Co}@N\text{-C}$ exhibited excellent electrocatalytic activity for OER, which can be attributed to the synergistic effect of Co, Mo_2C , and the graphitized structure of the N-doped carbon matrix. As is well known, the intrinsic activity of an electrode can be determined using its ECSA. The ECSA value of $\text{Mo}_2\text{C}/\text{Co}@N\text{-C}$ (0.032) was higher than that of $\text{Mo}_2\text{C}@N\text{-C}$ (0.013) according to the slope of the curve obtained through CV measurements of the $\text{Mo}_2\text{C}/\text{Co}@N\text{-C}$ catalyst at various scan rates (Figs. S5a–c). This indicated that the synergistic effect of Co and Mo_2C is an important factor governing the electrochemical reaction, although the physical porosity decreases because of the additional formation of Co particles inside the carbon matrix. The Nyquist plots of $\text{Mo}_2\text{C}/\text{Co}@N\text{-C}$ and $\text{Mo}_2\text{C}@N\text{-C}$ were obtained under OCV conditions to better understand the interfacial resistance to electron transfer during electrocatalysis, as shown in Fig. S5d. The $\text{Mo}_2\text{C}/\text{Co}@N\text{-C}$ catalyst had a smaller charge transfer resistance (R_{ct}) than that of $\text{Mo}_2\text{C}@N\text{-C}$, which is consistent with the previous catalyst

performance evaluation results. The long-term stability of $\text{Mo}_2\text{C}/\text{Co}@N\text{-C}$ was investigated at a constant current density of $10 \text{ mA}/\text{cm}^2$ for 12 h. As shown in Fig. 4c, a potential change of 60 mV was observed during the 12-h stability test, which indicated that $\text{Mo}_2\text{C}/\text{Co}@N\text{-C}$ exhibited excellent stability in the OER process.

The HER activities of $\text{Mo}_2\text{C}@N\text{-C}$, $\text{Mo}_2\text{C}/\text{Co}@N\text{-C}$, and Pt (20 wt%) were further evaluated in 0.1 M KOH (Fig. 4a). As shown in Fig. 4d, the $\text{Mo}_2\text{C}/\text{Co}@N\text{-C}$ catalyst required a potential of $-0.28 V_{\text{RHE}}$ to achieve $10 \text{ mA}/\text{cm}^2$, which is higher than that required by the 20 wt% Pt/C ($-0.18 V_{\text{RHE}}$) but lower than that required by $\text{Mo}_2\text{C}@N\text{-C}$ ($-0.49 V_{\text{RHE}}$). As mentioned above, the synergistic effect in the composite structure composed of Mo_2C , Co, and N-doped carbon is an important factor driving HER performance. In addition, stability measurements of $\text{Mo}_2\text{C}/\text{Co}@N\text{-C}$ were performed under $10 \text{ mA}/\text{cm}^2$ conditions for 12 h (Fig. 4f). They changed by only 12 mV over 12 h, which confirmed its excellent durability in HER applications. The excellent structure and carbon layer of the composite synthesized herein protect the Co and Mo_2C particles from alkaline corrosion, leading to the excellent durability results reported earlier in this paragraph. These results are comparable with previous studies (see Table S1). To evaluate the efficiency of the catalytic reactions, we performed a Tafel plot analysis showing the potential difference required to increase or decrease the current density. As shown in Figure S6, for OER, $\text{Mo}_2\text{C}/\text{Co}@N\text{-C}$ (164 mV/dec) showed a lower Tafel slope than commercial IrO_2 (180 mV/dec) and $\text{Mo}_2\text{C}@N\text{-C}$

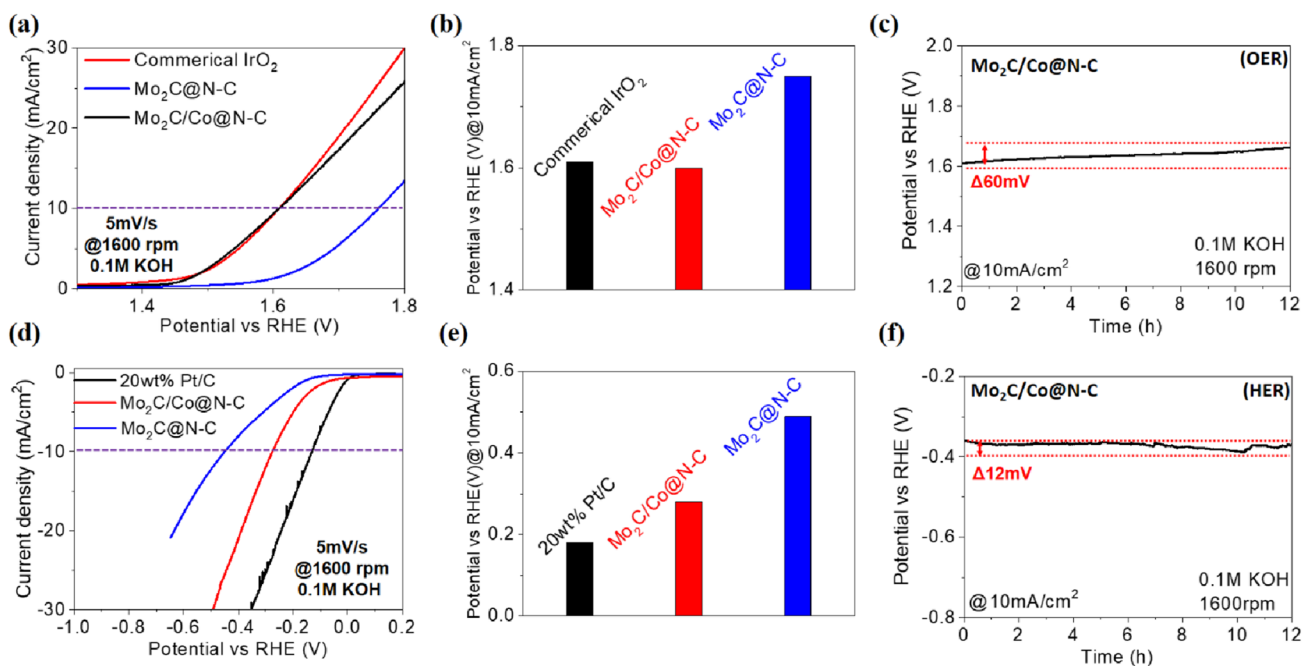


Fig. 4 LSV curves of various electrocatalysts at the rotation speed of 1600 rpm with a scan rate of 5 mV/s (a, d). Potential (vs. RHE) required to reach $10 \text{ mA}/\text{cm}^2$ (b, e). Stability test of $\text{Mo}_2\text{C}/\text{Co}@N\text{-C}$ sample at $10 \text{ mA}/\text{cm}^2$ for OER and HER (c, f)

(201 mV/dec), and for HER, Mo₂C/Co@N–C (126 mV/dec) showed a higher Tafel slope than 20 wt% Pt/C (115 mV/dec) but lower than Mo₂C@N–C (143 mV/dec). These results show a similar tendency to the LSV and ECSA results,

The enhanced OER and HER activities can be explained based on the following factors: (i) The higher surface area and pore volume of Mo₂C/Co@N–C with its larger surface area and pore volume provided sufficient contact between the active sites and the electrolyte to promote charge transfer. (ii) Mo₂C/Co@N–C with high Co–N and pyridine N contents were favorable for OER and HER. (iii) The low charge transfer resistance of Mo₂C/Co@N–C facilitated OER and HER kinetics, which was attributed to the synergistic effect of Co and Mo₂C encapsulated in the nitrogen-doped carbon matrix.

Conclusion

In this work, we developed a Mo₂C/Co@N–C catalyst with a corrugated hierarchical structure embedded in an N-doped carbon matrix. Co and Mo₂C nanoparticles, as HER and OER electroactive centers, respectively, were dispersed uniformly in the conductive nitrogen-doped carbon matrix and worked synergistically to enhance the OER and HER properties. Meanwhile, the carbon matrix formed in situ not only provided fast electron-transfer channels but also provided strong structural support for the corrosion and oxidation of Co and Mo₂C, thereby improving the overall water-splitting performance. The Mo₂C/Co@N–C catalyst exhibited good OER and HER performance, similar to that of precious metal catalysts, and it was stable for 12 h in 0.1 M KOH electrolyte. In sum, herein, we demonstrated a simple and feasible approach to fabricate robust and economical bifunctional electrocatalysts that are suitable for commercial water splitting as well as other applications related to energy storage and conversion.

Supplementary Information The online version contains supplementary material available at <https://doi.org/10.1007/s11814-024-00102-8>.

Acknowledgements This work was supported by the Creative Materials Discovery Program through the Ministry of Trade, Industry & Energy of Korea (MOTIE-20018989 and 20223030040220) and the Korea Institute of Science and Technology (2E32591). Also, this work was supported by the Korea Institute of Industrial Technology (EH230016)". Moreover, we thank Dr. Hyun S Park for the supervision of this study.

Data availability Data will be made available on request.

References

1. J. Song, C. Wei, Z.-F. Huang, C. Liu, L. Zeng, X. Wang, Z.J. Xu, *Chem. Soc. Rev.* **49**, 2196–2214 (2020)
2. J.S. Kim, B. Kim, H. Kim, K. Kang, *Adv. Energy Mater.* **8**, 1702774 (2018)
3. A. Kudo, Y. Miseki, *Chem. Soc. Rev.* **38**, 253–278 (2009)
4. W. Yang, R.R. Prabhakar, J. Tan, S.D. Tilley, J. Moon, *Chem. Soc. Rev.* **48**, 4979–5015 (2019)
5. B.M. Hunter, H.B. Gray, A.M. Muller, *Chem. Rev.* **116**, 14120–14136 (2016)
6. L. Gao, X. Cui, C.D. Sewell, J. Li, Z. Lin, *Chem. Soc. Rev.* **50**, 8428–8469 (2021)
7. S. Li, Y. Gao, N. Li, L. Ge, X. Bu, P. Feng, *Energy Environ. Sci.* **14**, 1897–1927 (2021)
8. H.-F. Wang, L. Chen, H. Pang, S. Kaskel, Q. Xu, *Chem. Soc. Rev.* **49**, 1414–1448 (2020)
9. A. Zhang, Y. Liang, H. Zhang, Z. Geng, J. Zeng, *Chem. Soc. Rev.* **50**, 9817–9844 (2021)
10. M. Tahir, L. Pan, F. Idrees, X. Zhang, L. Wang, J.-J. Zou, Z.L. Wang, *Nano Energy* **37**, 136–157 (2017)
11. H. Xu, H. Shang, C. Wang, Y. Du, *Coord. Chem. Rev.* **418**, 213374 (2020)
12. Z. Kou, Y. Yu, X. Liu, X. Gao, L. Zheng, H. Zou, Y. Pang, Z. Wang, Z. Pan, J. He, *ACS Catal.* **10**, 4411–4419 (2020)
13. T. Ouyang, Y.Q. Ye, C.Y. Wu, K. Xiao, Z.Q. Liu, *Angew. Chem. Int. Ed.* **58**, 4923–4928 (2019)
14. M. Li, Y. Zhu, H. Wang, C. Wang, N. Pinna, X. Lu, *Adv. Energy Mater.* **9**, 1803185 (2019)
15. R.A. Mir, O.P. Pandey, *Chem. Eng. J.* **348**, 1037–1048 (2018)
16. J. Dong, Q. Wu, C. Huang, W. Yao, Q. Xu, *J. Mater. Chem. A* **6**, 10028–10035 (2018)
17. H. Yu, S. Xie, J. Yang, J. Lv, W. Tan, J. Yin, J. Wang, M. Zhao, C. Wang, M. Zhang, *Colloids Surf A Physicochem Eng Asp* **645**, 128953 (2022)
18. Z.-Y. Yu, Y. Duan, M.-R. Gao, C.-C. Lang, Y.-R. Zheng, S.-H. Yu, *Chem. Sci.* **8**, 968–973 (2017)
19. L. Xia, X. Zhang, H. Song, Y. Zheng, X. Li, B. Gao, K. Huo, P.K. Chu, *Int. J. Hydrogen Energy* **45**, 22629–22637 (2020)
20. Q. Liang, H. Jin, Z. Wang, Y. Xiong, S. Yuan, X. Zeng, D. He, S. Mu, *Nano Energy* **57**, 746–752 (2019)
21. S. Cui, M. Li, X. Bo, *Int. J. Hydrogen Energy* **45**, 21221–21231 (2020)
22. K. An, X. Xu, *Electrochim. Acta* **293**, 348–355 (2019)
23. D. Reynard, B. Nagar, H. Girault, *ACS Catal.* **11**, 5865–5872 (2021)
24. C. Lu, D. Tranca, J. Zhang, F.N. Rodríguez Hernández, Y. Su, X. Zhuang, F. Zhang, G. Seifert, X. Feng, *ACS Nano* **11**, 3933–3942 (2017)
25. H. Ren, Y. Zhang, L. Liu, Y. Li, D. Wang, R. Zhang, W. Zhang, Y. Li, B.-C. Ye, *Microchim. Acta* **186**, 1–9 (2019)
26. H. Wei, J. Wang, Q. Lin, Y. Zou, X.A. Chen, H. Zhao, J. Li, H. Jin, Y. Lei, S. Wang, *Nano Energy* **86**, 106047 (2021)
27. D.K. Sam, S. Gong, A. Durairaj, E.K. Sam, J. Liu, X. Lv, *Int. J. Energy Res.* **45**, 10989–11001 (2021)
28. W. Yaseen, M. Xie, B.A. Yusuf, Y. Xu, N. Ullah, M. Rafiq, A. Ali, J. Xie, *Appl. Surf. Sci.* **579**, 152148 (2022)
29. Y. Liu, X. Zhu, Q. Zhang, T. Tang, Y. Zhang, L. Gu, Y. Li, J. Bao, Z. Dai, J.-S. Hu, *J. Mater. Chem. A* **8**, 8920–8926 (2020)
30. H.Q. Chang, G.H. Zhang, K.-C. Chou, *Electrochim. Acta* **394**, 139119 (2021)
31. Y. Wang, K. Li, F. Yan, C. Li, C. Zhu, X. Zhang, Y. Chen, *Nanoscale* **11**, 12563–12572 (2019)
32. S. Yuan, M. Xia, Z. Liu, K. Wang, L. Xiang, G. Huang, J. Zhang, N. Li, *Chem. Eng. J.* **430**, 132697 (2022)
33. P. Zhang, Y. Liu, T. Liang, E.H. Ang, X. Zhang, F. Ma, Z. Dai, *Appl. Catal. B* **284**, 119738 (2021)
34. J. Zhang, X.P. Sun, P. Wei, G. Lu, S.X. Sun, Y. Xu, C. Fang, Q. Li, J.T. Han, *ChemCatChem* **12**, 3737–3745 (2020)

35. X. Luo, Q. Zhou, S. Du, J. Li, J. Zhong, X. Deng, Y. Liu, A.C.S. Appl. Mater. Interfaces **10**, 22291–22302 (2018)
36. M.H. Gomaa, Z.A. Hamid, M.A.M. Ibrahim, R.A. El Sttar, E.-S.H. El-Mosallamy, Korean J. Chem. Eng. **40**, 1186–1196 (2023)
37. Y. Shi, J. Cai, X. Zhang, Z. Li, S. Lin, Int. J. Energy Res. **47**, 7761–7769 (2022)
38. X. Hou, H. Zhou, M. Zhao, Y. Cai, Q. Wei, ACS Sustain. Chem. Eng. **8**, 5724–5733 (2020)
39. S. Ghosh, S.M. Jeong, S.R. Polaki, Korean J. Chem. Eng. **35**, 1389–1408 (2018)
40. J.B. Hwang, S. Kim, W.-S. Chae, H.M. Pathan, M.A. Mahadik, J.S. Jang, Korean J. Chem. Eng. **38**, 1149–1160 (2021)
41. H.S. Kim, M.S. Kang, W.C. Yoo, J. Phys. Chem. C **119**, 28512–28522 (2015)
42. J. Lee, H.S. Kim, J.-H. Jang, E.-H. Lee, H.-W. Jeong, K.-S. Lee, P. Kim, S.J. Yoo, ACS Sustain. Chem. Eng. **9**, 7863–7872 (2021)
43. H.S. Kim, M. Kim, M.S. Kang, J. Ahn, Y.-E. Sung, W.C. Yoo, ACS Sustain. Chem. Eng. **6**, 2324–2333 (2018)
44. K.-H. Kim, Y.-J. Song, H.-J. Ahn, Korean J. Chem. Eng. **40**, 1071–1076 (2023)
45. Y. Sohn, D.-G. Kim, J.H. Lee, S. Lee, I.S. Hwang, S.-H. Lee, S.J. Yoo, P. Kim, Korean J. Chem. Eng. **37**, 938–945 (2020)

Publisher's Note Springer Nature remains neutral with regard to jurisdictional claims in published maps and institutional affiliations.

Springer Nature or its licensor (e.g. a society or other partner) holds exclusive rights to this article under a publishing agreement with the author(s) or other rightsholder(s); author self-archiving of the accepted manuscript version of this article is solely governed by the terms of such publishing agreement and applicable law.